Modelling confined hydrogen–air detonations with the conservation element/solution element method for varying initial compositions

Martins, Simão M.; Zuijlen, Alexander van; Castro, Saullo G.P.

DOI
10.1016/j.psep.2025.108257

Publication date
2026

Document Version
Final published version

Published in
Process Safety and Environmental Protection

Process Safety and Environmental Protection 206 (2026) 108257

Contents lists available at ScienceDirect

Process Safety and Environmental Protection

journal homepage: www.elsevier.com/locate/psep

Modelling confined hydrogen–air detonations with the conservation element/solution element method for varying initial compositions

Simão M. Martins [a,*], Alexander van Zuijlen [b], Saullo G.P. Castro [a,*]

[a] Department of Aerospace Structures and Materials, Delft University of Technology, Kluyverweg 1, Delft, 2629 HS, Netherlands
[b] Department of Flow Physics and Technology, Delft University of Technology, Kluyverweg 1, Delft, 2629 HS, Netherlands

ARTICLE INFO

Keywords:
Hydrogen detonation
CESE method
Blast loads
Variable composition
Confinement
Finite-rate chemistry

ABSTRACT

Hydrogen transportation poses significant explosion risks, especially under confined conditions. This study evaluates the accuracy of the Conservation Element/Solution Element (CESE) method, with finite-rate chemistry, for predicting blast loads from confined hydrogen–air detonations at varying initial compositions. A shock tube simulation is compared against one-dimensional theory at the detonation front, using four reaction mechanisms (7 to 19 species). The 7-species mechanism predicts the Chapman–Jouguet (CJ) state within 1%–2% error up to 40 vol% H_2, offering a computationally efficient option for large simulations, considering that computational time scales with the square of the number of species. While mesh refinement (0.2–2 mm) improves peak pressure prediction, impulse remains 5% underestimated due to the unresolved induction zone. The proposed 2D model – using 7 species, 1 mm mesh size and inviscid flow – is then validated against a confined detonation experiment from literature. It accurately predicts detonation speed, pressure history (including shock reflections), and impulse along the 3-metre chamber. The study provides insight into the applicability and limitations of the CESE-chemistry method in confined detonation scenarios.

1. Introduction

Hydrogen has the potential to become a clean energy carrier with a central role in achieving net-zero CO_2 emissions by 2050 (Evro et al., 2024; IEA, 2023). According to the International Energy Agency, meeting this scenario would require around 388 million tonnes of low-emission hydrogen by then, with major applications in aviation, shipping, road transportation, and power generation (IEA, 2023).

However, hydrogen's wide flammability range (4–75 vol%), low ignition energy, high volatility, and high flame speeds pose significant safety concerns (Wen et al., 2025). A statistical analysis based on the HIAD 2.0 database, including 576 hydrogen-related incidents, found that ignition occurred in 79% of the cases and 48% resulted in explosion (Wen et al., 2022).

Detonations represent a worst-case explosion scenario in hydrogen safety due to their high pressures, high temperatures, and supersonic blast waves reaching speeds around 2000 m/s (Chamberlain et al., 2019; Groethe et al., 2007). Detonability limits of hydrogen in air are typically quoted within 18–59 vol% (Wen et al., 2025), although experiments with large confined volumes report deflagration-to-detonation transition (DDT) happening for concentrations as low as 12.5 vol% (Dorofeev et al., 1996). Confined environments increase the risk of hydrogen accumulation, DDT, and shock wave reflections, which can amplify their destructive effects (Rokhy and Soury, 2022; Chamberlain et al., 2019; Groethe et al., 2007). A notable example of this is the 2011 Fukushima nuclear plant catastrophe (Yanez et al., 2015). DDT occurs in confined environments due to turbulence and obstacles in the flame path, causing shocks to develop and interact with the reaction front, eventually leading to a detonation onset (Oran and Gamezo, 2007; Wen et al., 2025; Hasslberger et al., 2015).

Given the destructive potential of hydrogen detonations, numerical modelling stands as a safe and cost-effective way to assess hazards and structural impact in early design stages.

1.1. One-dimensional detonation front

A detonation is a supersonic shock wave coupled with a reaction zone. In one dimension, the leading shock compresses the unburned mixture, causing a sharp rise in pressure and temperature that initiates chain-branching reactions. This corresponds to the von Neumann (vN) state, where pressure reaches its maximum value, denominated P_{vN}, but significant reactions have not yet occurred. (Fickett and Davis, 2000).

After a finite induction time, exothermic reactions release chemical energy, further increasing the temperature and driving gas expansion. As chemical equilibrium is reached – the Chapman–Jouguet (CJ) state –, temperature stabilises at T_{CJ}, and the pressure drops to P_{CJ}.

* Corresponding authors.
E-mail addresses: S.M.Martins@tudelft.nl (S.M. Martins), A.H.vanZuijlen@tudelft.nl (A. van Zuijlen), S.G.P.Castro@tudelft.nl (S.G.P. Castro).

https://doi.org/10.1016/j.psep.2025.108257
Received 2 October 2025; Received in revised form 1 December 2025; Accepted 1 December 2025
Available online 2 December 2025

A self-sustained detonation propagates at the theoretical CJ speed, V_{CJ}, where the flow behind its front becomes sonic and acoustic perturbations can no longer affect the shock (Fickett and Davis, 2000).

The vN and CJ states are solutions to the Rankine–Hugoniot jump conditions, assuming frozen and equilibrium compositions, respectively. Intermediate states are described by the Zeldovich–von Neumann–Döring (ZND) model, which solves the Euler equations for a one-dimensional, planar, and steady wave (Fickett and Davis, 2000; Browne et al., 2024).

The ZND model is implemented in the Shock and Detonation Toolbox developed by Caltech (Browne et al., 2024), incorporating chemical kinetics to compute the spatial profiles of pressure, temperature, and species mass fractions across the detonation front.

1.2. Modelling approaches for detonation blast loads

Blast loading from detonations can be predicted with different levels of fidelity, depending on the application.

The TNT equivalence method is widely used to estimate blast loads for structural analysis (United States Department of the Army, 1986; Kim et al., 2023). Assuming an efficiency factor η, one can convert the energy of a gas explosion, such as H_2-air, into an equivalent mass of TNT to obtain semi-empirical blast pressure curves at a given stand-off distance. Alternatively, the equivalent TNT mass can be modelled in an Eulerian mesh with a burn fraction controlling the detonation energy release and an equation of state – typically the Jones-Wilkins-Lee (JWL EOS) – to describe the TNT products' expansion (Chen et al., 2023; Rokhy and Mostofi, 2023).

Although computationally efficient, since chemical kinetics is not included, these methods are sensitive to the choice of η, which must be tuned to each case and geometry (Chen et al., 2023; Kim et al., 2023). Furthermore, they are mostly applied to open-field scenarios where the pressure is measured away from the detonation point. For confined detonation scenarios, with wall shock interactions and possible mixture inhomogenities, it is necessary to incorporate chemical kinetics in the model.

Simulations with detailed finite-rate chemistry can capture the cellular structure of H_2 detonations and triple points resulting from the interaction between the flame front and transverse waves (Sharpe, 2001; Smirnov et al., 2024; Sankar et al., 2025; Weng et al., 2025). However, to resolve the chemical induction scales, the mesh sizes are in the order of micrometres, making it computationally unfeasible for full-scale safety analysis.

Hasslberger et al. modelled H_2-air DDT in a large confined volume using under-resolved meshes (Hasslberger et al., 2015). They employed adaptive mesh refinement (AMR) techniques to achieve higher resolution near the precursor shocks and flame tip, allowing to predict flame acceleration and DDT by shock focusing.

AMR functionality, however, is often limited or unavailable in commercial fluid–structure interaction (FSI) solvers required for structural analysis. To address computational efficiency, we use under-resolved fixed meshes, a reduced reaction mechanism, and assume 2D planar-wave conditions, which are compatible with FSI frameworks.

For this purpose, the Conservation Element/Solution Element (CESE) method, implemented in LS-DYNA (Grippon et al., 2015), is employed along with finite-rate chemistry. LS-DYNA is chosen for its integrated structural and reacting flow capabilities, within a single framework, allowing extension to future FSI studies (Rokhy and Mostofi, 2023; Haghgoo et al., 2021; Grippon et al., 2015).

Originally proposed by Chang (1995), CESE is a second-order, explicit scheme that differs significantly from traditional finite-volume methods (FVM), due to (Jiang et al., 2020):

- Unified treatment of space and time.
- Introduction of conservation elements (CE) and solution elements (SE) to discretise the space–time domain.
- Physical variables approximated by a Taylor expansion inside each SE, and conservation equations enforced at each CE.
- Use of a compact stencil, requiring only neighbouring cell information, which favours parallelisation.
- Spatial derivatives of the physical quantities are stored and updated as independent variables.

The above features result in low dissipation and high compactness, achieving accurate solutions even with CFL numbers close to 1 (Chang, 1995; Grippon et al., 2015). In a study by Jiang et al. (2020), the Sod's shock-tube problem was solved by the CESE method and an FVM using the monotonic upstream-centred scheme (MUSCL). The CESE method better resolved the narrow shock discontinuities while showing superior computational efficiency.

Im et al. studied H_2-O_2-Ar detonations in a shock tube using the CESE approach with a 9-species reaction mechanism (Im et al., 2002). The detonation CJ properties and temporal evolution were closely aligned with previous numerical and experimental results.

The LS-DYNA-based CESE solver has been used in FSI studies, to model metal forming under H_2-O_2 detonations (Haghgoo et al., 2021; Rokhy and Soury, 2019), the response of concrete barriers to H_2-air blasts (Rokhy and Mostofi, 2023), and confinement effects in propane detonations (Rokhy and Soury, 2022). Compared to the TNT method, it captured more accurately load duration, the negative pressure phase, and total impulse, particularly in semi-confined detonations (Rokhy and Mostofi, 2023; Chen et al., 2023).

The present study evaluates the capability of the CESE-chemistry method to predict H_2-air detonations under concentrations ranging from 20 to 55 vol%. The impact of under-resolved mesh, reduced reaction mechanisms, and 2D planar wave conditions on the blast loading is discussed. To quickly evaluate the effects on the detonation front and computational effort, a shock-tube detonation is first modelled. Finally, with an efficient choice of reaction mechanism and mesh size, the method is validated against a full-scale confined detonation experiment, demonstrating its applicability and limitations in a complex scenario.

2. Methodology

Fig. 1 illustrates the proposed verification and validation strategy for the CESE-chemistry method. The first verification consists of a shock-tube detonation case, for which the results can be compared against the one-dimensional ZND model (Browne et al., 2024).

The proposed model is then validated against a full-scale hydrogen–air detonation experiment, performed for various H_2 concentrations, from Rudy et al. (2017), who recorded the pressure–time data at multiple locations, showing complex shock reflections in a confined chamber.

2.1. Shock tube model

The computational domain consists of a long and narrow shock tube ($\varnothing 0.01 \times 1$ m) modelled in 2D using a structured mesh. The initial conditions are $P_0 = 1$ bar, $T_0 = 300$ K, and a H_2-air mixture varying between 20–55 vol% of H_2.

Direct ignition is numerically triggered by creating a planar high-pressure region ($P_i = 1.5$ MPa), immediately followed by a high-temperature region ($T_i = 3000$ K), each 2 mm thick, at the left end of the tube (see Fig. 2). The rapid expansion of compressed gas generates a strong shock that couples with reactions initiated in the high-temperature region. Following a brief acceleration phase, the detonation stabilised at the Chapman–Jouguet speed V_{CJ}, allowing direct comparison with the ZND solution computed using the Shock and Detonation Toolbox (Browne et al., 2024).

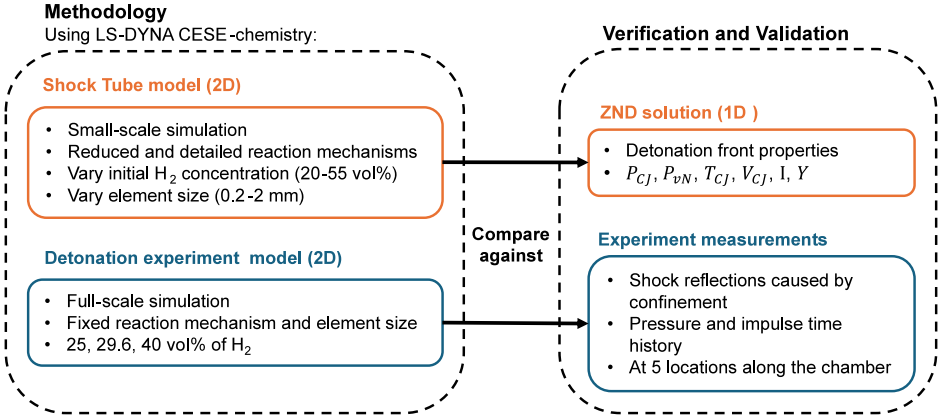

Fig. 1. Methodology and validation plan.

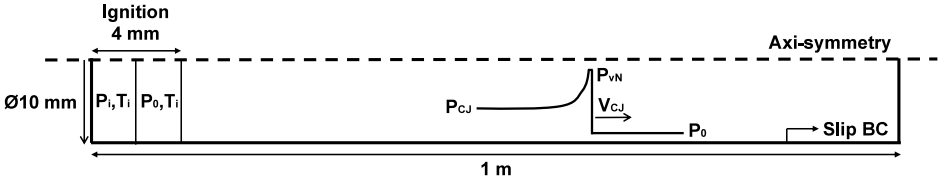

Fig. 2. 2D shock tube model and detonation wave travelling from left to right (not at scale).

2.1.1. Compressible CFD solver

Due to the high propagation speeds of detonation waves, reaction timescales are much smaller than diffusion ones, allowing us to neglect diffusive effects for practical purposes (Fickett and Davis, 2000). The flow is governed by the inviscid, compressible Euler equations for mass, momentum, and energy conservation (Eqs. (1a)–(1c)), extended with species mass conservation (Eq. (1d)) to describe chemically reacting flows (Poinsot and Veynante, 2005):

$$\frac{\partial \rho}{\partial t} + \frac{\partial}{\partial x_i}(\rho u_i) = 0 \tag{1a}$$

$$\frac{\partial}{\partial t}(\rho u_j) + \frac{\partial}{\partial x_i}(\rho u_i u_j) + \frac{\partial p}{\partial x_j} = 0 \tag{1b}$$

$$\frac{\partial}{\partial t}(\rho E) + \frac{\partial}{\partial x_i}(u_i[\rho E + p]) = 0 \tag{1c}$$

$$\frac{\partial}{\partial t}(\rho Y_k) + \frac{\partial}{\partial x_i}(\rho u_i Y_k) = \dot{\omega}_k \tag{1d}$$

Here, ρ is the density, u_i is the velocity component in direction x_i, p is the pressure, $E = e + \frac{1}{2}u_i u_i$ is the specific total energy, Y_k is the mass fraction of species k, and $\dot{\omega}_k$ is its production rate.

At high initial pressures, the ideal gas EOS underpredicts CJ speed, pressure, and temperature for hydrogen detonations (starting from 5–10 bar) (Schmitt and Butler, 1995; Weng and Mével, 2022), and it also yields larger detonation cell sizes compared with real gas models (Weng et al., 2025). In this work, however, the initial pressure is 1 bar, for which ideal gas and real gas EOS provide similar results. For this reason, the ideal gas law was adopted.

The CESE solver is used to solve the reacting flow. For the shock-tube verification, the geometry is assumed 2D axi-symmetric, with the axis of symmetry being along the tube length, and slip boundary conditions are applied to the walls (see Fig. 2).

The explicit time step is governed by the Courant–Friedrichs–Lewy (CFL) condition, requiring $C_{\mathrm{CFL}} \leq 1$ for stability. A Courant number $C_{\mathrm{CFL}} = 0.99$ provides stable, non-oscillatory results while maximising efficiency Appendix A. Lower $C_{\max}$ values increase numerical dissipation and degrade shock resolution by smearing the discontinuity (Wen et al., 2023). The CESE solver incorporates a relaxation procedure with some numerical dissipation, controlled by a parameter $\epsilon \geq 0$. Values of $\epsilon \geq 0.5$ yield stable solutions Appendix A, with larger values enhancing stability at the cost of accuracy (ANSYS, Inc., 2024).

2.1.2. Reaction mechanisms

Hydrogen combustion involves intermediate species, or radicals, that are first generated through initiating reactions (mainly from No. 10 in Table 1). These radicals (OH, H, O, HO_2, H_2O_2) propagate the chain reactions and recombine to form stable products, like H_2O, releasing energy that sustains the detonation (Warnatz et al., 1996).

Reaction rates are governed by temperature-dependent Arrhenius kinetics, being strongly coupled with fluid flow. For each reaction j, the forward rate constant is defined as (Poinsot and Veynante, 2005):

$$K_{f,j} = A_j\, T^{\beta_j}\, \exp\left(-\frac{E_j}{RT}\right) \tag{2}$$

where A_j, β_j, and E_j are the Arrhenius pre-exponential factor, temperature exponent, and activation energy, respectively; R is the universal gas constant and T is the temperature. The net species production rate $\dot{\omega}_k$ is computed by summing the contributions of all M reactions:

$$\dot{\omega}_k = W_k \sum_{j=1}^{M} (\nu''_{kj} - \nu'_{kj})\, Q_j \tag{3a}$$

$$Q_j = K_{f,j} \prod_{k=1}^{N} [X_k]^{\nu'_{kj}} - K_{r,j} \prod_{k=1}^{N} [X_k]^{\nu''_{kj}} \tag{3b}$$

with W_k being the molecular weight of species k; $[X_k]$ the molar concentration; and ν'_{kj}, ν''_{kj} the forward and reverse stoichiometric coefficients. The production rate $\dot{\omega}_k$ is the source term in Eq. (1d). Its evaluation requires a predefined reaction mechanism, including N species, M reactions, and their kinetic parameters. These are given to LS-DYNA in the CHEMKIN format.

Olm et al. (2014) assessed the performance of 19 hydrogen reaction mechanisms against shock-tube data over a wide range of conditions relevant to detonations. More recent work by Huang et al. (2025)

Table 1
H_2-air Kéromnès mechanism with 10[b] species and 19 reactions (complete description with third-body efficiencies and falloff reactions in Kéromnès et al., 2013). Units: cm^3/mol/s/cal.

No.	Reaction	*A*	*β*	*E*
1[a]	$H + O_2 = O + OH$	1.040E+14	0.00	1.529E+4
2[a]	$O + H_2 = H + OH$	5.080E+04	2.67	6.292E+3
3[a]	$OH + H_2 = H + H_2O$	4.380E+13	0.00	6.990E+3
4[a]	$O + H_2O = OH + OH$	2.970E+06	2.02	1.340E+4
5[a]	$H_2 + M = H + H + M$	4.577E+19	−1.40	1.044E+5
6[a]	$O + O + M = O_2 + M$	6.165E+15	−0.50	0.00
7[a]	$O + H + M = OH + M$	4.714E+18	−1.00	0.00
8[a]	$H + OH + M = H_2O + M$	3.500E+22	−2.00	0.00
9	$H + O_2 (+M) = HO_2 (+M)$	4.650E+12	0.44	0.00
10	$H_2 + O_2 = H + HO_2$	5.176E+05	2.43	5.350E+4
11	$HO_2 + H = OH + OH$	7.079E+13	0.00	2.950E+02
12	$HO_2 + O = OH + O_2$	3.250E+13	0.00	0.00
13	$HO_2 + OH = H_2O + O_2$	2.456E+13	0.00	−4.970E+2
14a	$HO_2 + HO_2 = H_2O_2 + O_2$	1.300E+11	0.00	−1.630E+3
14b	$HO_2 + HO_2 = H_2O_2 + O_2$	3.658E+14	0.00	1.200E+4
15	$H_2O_2 (+M) = OH + OH (+M)$	2.000E+12	0.90	4.875E+4
16	$H_2O_2 + H = H_2O + OH$	2.410E+13	0.00	3.970E+3
17	$H_2O_2 + H = H_2 + HO_2$	2.150E+10	1.00	6.000E+3
18	$H_2O_2 + O = OH + HO_2$	9.550E+06	2.00	3.970E+3
19a	$H_2O_2 + OH = H_2O + HO_2$	1.740E+12	0.00	3.180E+2
19b	$H_2O_2 + OH = H_2O + HO_2$	7.590E+13	0.00	7.269E+3

[a] The first 8 reactions and 7 species, with different coefficients, correspond to the Evans et al. mechanism (Evans and Schexnayder, 1980).
[b] 10 species: H, O, OH, H_2, O_2, H_2O, N_2 (bath gas), HO_2, H_2O_2, Ar (third body).

presented combined reaction mechanisms that include nitrogen chemistry and evaluated them based on dynamic detonation parameters and ignition delay times, while Sankar et al. (2025) analysed four mechanisms with focus on detonation cell size.

In the present study, two detailed hydrogen–air mechanisms are selected. The mechanism from Kéromnès et al. (2013) (Table 1), with 10 species and 19 reactions, is selected for computing the ZND solution since it performed the best in the comparative study by Olm et al. (2014). GRI-Mech 3.0 (Smith et al., 1999), with 19 species and 70 reactions, includes additional NO_x chemistry. Both mechanisms include falloff reactions. Hydrocarbon species, irrelevant to the present study, are excluded.

To decrease computational cost, since each species requires solving an additional mass equation (Eq. (1d)), two reduced mechanisms applicable to supersonic hydrogen flames are also considered. The first, by Evans and Schexnayder (1980) (Table B.4 in Appendix B), includes 7 species and 8 reactions. The second, by Drummond et al. (1986) (Table B.5 in Appendix B), includes 7 reactions. Both omit HO_2 and H_2O_2, which are primarily relevant at low temperatures (Evans and Schexnayder, 1980).

In the reduced mechanisms, air is assumed to be a binary O_2-N_2 mixture, while the detailed mechanisms also include Ar. Nitrogen is treated as inert, except in GRI-Mech 3.0, where it participates in NO_x formation. Table 1 summarises the detailed Kéromnès mechanism, used as a reference. The first 8 reactions are similar to the Evans mechanism, but with different coefficients.

2.1.3. Thermodynamic properties

Under the ideal gas assumption, the internal energy e (appearing in Eq. (1c)) depends only on the temperature and is related to the heat capacity of each species at constant pressure, $C_{pk}(T)$.

The heat capacity $C_{pk}(T)$ is expressed using the NASA-polynomial form, which fits data over a wide temperature range using two separate intervals (200–1000 K and 1000–6000 K) (Mcbride et al., 1993). Each range is described by 7 coefficients a_{nk}: with the first five directly defining C_{pk} as per Eq. (4); whereas the remaining two are used to compute species enthalpy and entropy.

$$\frac{C_{pk}}{R} = a_{1k} + a_{2k}T + a_{3k}T^2 + a_{4k}T^3 + a_{5k}T^4 \tag{4}$$

All coefficients (listed in Appendix C) are sourced from the Explosion Dynamics Laboratory (Browne et al., 2024), which was adapted from NASA Glenn thermodynamic reports (Mcbride et al., 1993). These are also given to LS-DYNA in the CHEMKIN format.

2.2. Reproducing a confined hydrogen detonation experiment

To validate the CESE-chemistry method in a more complex scenario, we reproduce a hydrogen detonation experiment conducted by Rudy et al. (2017). The experimental setup consisted of a closed chamber with an acceleration section (0.11 m × 0.11 m × 1 m) filled with an H_2-air mixture, followed by a test section (0.11 m × 0.075/0.085 m × 2 m). The test section contained air on the lower half (blue region in Fig. 3) and H_2-air mixture on the upper half (red region), separated by a thin membrane.

In the experiment, ignition occurred at the left end of the chamber. The detonation wave travelled through a 0.35 m turbulence generator that induces a deflagration-to-detonation transition (DDT), and continued through the remainder of the acceleration section. By the time it entered the test section, the detonation was fully developed (Rudy et al., 2017).

Five high-frequency pressure sensors (PS1 to PS5) were installed along the upper wall at distances L = 0.74, 1.17, 1.65, 2.13, and 2.60 m from the ignition point. These sensors recorded pressure–time histories, which are used to compare with numerical results. Measurements were conducted for three mixture compositions: 25 vol% (lean), 29.6 vol% (stoichiometric), and 40 vol% (rich) of H_2.

2.2.1. Numerical model setup

The detonation chamber, shown in Fig. 3, is modelled as a 2D planar geometry, assuming inviscid flow and slip boundary conditions, similar to the shock tube simulations. These simplifications significantly reduce computational cost, enabling full-scale simulations. The mesh size and reaction mechanism are later selected based on the results in Section 3.1.

Direct ignition is triggered at the yellow region in Fig. 3, as described already in Section 2.1. Shortly after, a self-sustained, planar detonation wave is formed. Since DDT is bypassed in the model, the acceleration section length was shortened to 0.7 m (instead of 1 m) to calibrate the impulse history at PS1. This was achieved by running simulations with a 0.6–0.8 m section and calculating the impulse error with respect to the stoichiometric experiment. With 0.7 m, this error is below 1%, increasing to 6% for 0.6 m and 8% for 0.8 m.

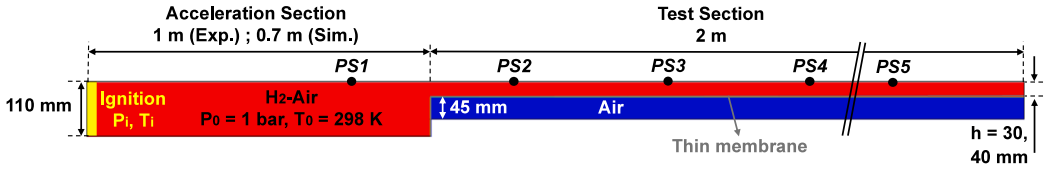

Fig. 3. LS-DYNA model of the detonation chamber, showing the acceleration and test sections (not at scale).

The initial conditions are set to P_0 = 1 bar and T_0 = 298 K throughout the domain (except in the ignition zone), with varying H_2-air compositions (25, 29.6, and 40 vol% of H_2). A thin membrane (0.1 mm), modelled with shell elements and a soft material, is included between the air and H_2-air regions to prevent mixing. When the membrane elements reach a maximum pressure P_{max} = 0.2 MPa (in compression), upon the arrival of the detonation front, they are deleted without influencing the flow. This failure criterion is defined in LS-DYNA using the "MAT_ADD_EROSION" keyword.

3. Results and discussion

3.1. Shock tube

This section compares the shock tube simulation results with the ZND solution, focusing on the detonation front. The objective is to understand how accurately the CESE-chemistry method captures key one-dimensional detonation features under varying reaction mechanisms and initial conditions.

Time–history data, from the CESE model, is extracted at 0.9 m along the tube. The Chapman–Jouguet (CJ) point – representing the equilibrium state – was defined 10 μs after the shock arrival, when the rate of change in pressure (dP/dt) is below 1% of the maximum rate $(dP/dt)_{\max}$, for all tested compositions. Temperature stabilises earlier than pressure.

The specific impulse I is the integral of the overpressure, i.e. $\int (P - P_0)\, dt$.

3.1.1. Reaction mechanisms comparison

Fig. 4 presents the temperature (T), pressure (P), specific impulse (I), and species mass fractions (Y) across the detonation front, using both detailed (Kéromnès, GRI-Mech 3.0) and reduced (Evans, Drummond) mechanisms.

In the ZND results (black line), a shock wave travelling at V_{CJ} = 1972 m/s instantaneously compresses the unreacted gases to P_{vN} = 2.77 MPa and T_{vN} = 1543 K. After a short induction time (Δt = 0.54 μs), exothermic reactions release energy and raise the temperature further, while pressure decreases due to expansion. This coincides with the peak OH formation in Fig. 4(c). At the equilibrium CJ state, pressure and temperature are P_{CJ} = 1.55 MPa and T_{CJ} = 2961 K, respectively.

Note that this is a solution of the detonation front only, with no consideration for the trailing Taylor–Zeldovich expansion wave, which would decrease both P and T beyond the CJ point (Browne et al., 2024).

The CESE-chemistry simulations reproduce the ZND trends well. Both detailed and reduced mechanisms yield similar results under stoichiometric conditions, with only minor deviations in OH formation for GRI-Mech 3.0 (Fig. 4(c)). Predicted values of V_{CJ} (1983–1990 m/s), T_{CJ}, and P_{CJ} match the ZND solution within 1%–2% error (Fig. 5). However, peak pressure P_{vN} is under-predicted by 8%–12%, mainly due to mesh resolution limitations, as discussed further in Section 3.1.3.

Specific impulse I is a critical parameter in structural blast loading (Hetherington and Smith, 2014). At 10 μs after the shock, the CESE solution yields an impulse 3%–4% below the ZND result (Fig. 5). That is because the CESE solutions do not exhibit a well-defined induction zone. Exothermic reactions begin immediately after the shock, as shown

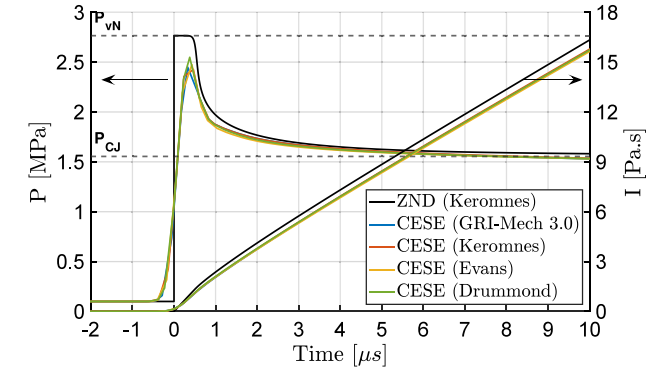

(a) Pressure (left) and specific impulse (right).

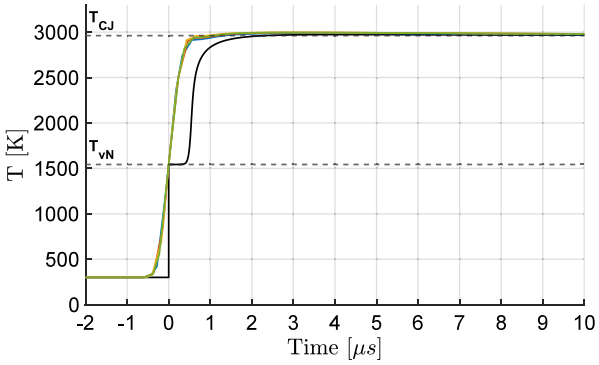

(b) Temperature.

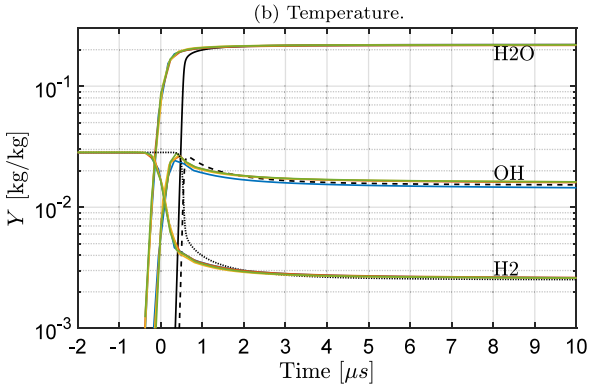

(c) Mass fractions.

Fig. 4. Comparison between CESE and ZND detonation front solutions using several reaction mechanisms. Stoichiometric H_2-air mixture at P_0 = 1 bar, T_0 = 300 K.

by the significant presence of H_2O at t = 0 μs (Fig. 4(c)). This premature energy release prevents the pressure and temperature from remaining constant during the shock-compressed von Neumann (vN) state, leading to an underestimated impulse in this region.

The induction length, defined as the distance between the shock front and the point of maximum temperature gradient in the ZND solution, is Δ_i=0.2 mm under stoichiometric conditions. Several points are required along the induction zone to capture it correctly (Sharpe,

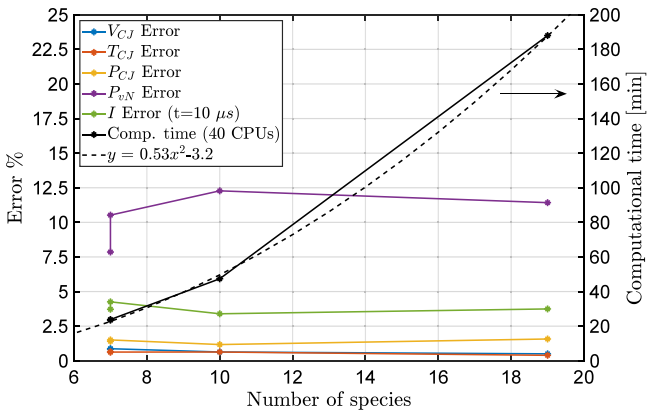

Fig. 5. Errors relative to the ZND solution vs. the number of species, and respective computational time.

2001). Such fine resolution is computationally prohibitive in large simulations, leaving the induction zone unresolved, which reflects on an artificially premature ignition. Note that the smallest step used by the ZND solver was 2 μm.

As shown in Fig. 5, CESE computational cost increases with the square of the number of species, consistent with Im (2018). Reduced mechanisms (Evans and Drummond), each using 7 species, are approximately 2 to 8 times faster than the detailed mechanisms (Kéromnès and GRI-Mech 3.0, respectively). Given their computational efficiency and comparable accuracy in reproducing 1D detonation characteristics, these reduced mechanisms are well-suited for larger simulations.

3.1.2. Effect of initial composition

To evaluate how the CESE-chemistry method captures detonation properties across different mixture compositions, simulations were performed with H_2 concentrations ranging from 20–55 vol% – within the detonability limits. Both reduced (Evans) and detailed (Kéromnès) mechanisms were tested under initial conditions of P_0 = 1 bar and T_0 = 300 K. The resulting CJ temperature, speed, pressure, and impulse are shown in Fig. 6.

While T_{CJ} remains constant (within 0.2%), P_{CJ} is more sensitive to the selection of the CJ point (at 10 μs), varying about 2% between 10 ± 2 μs. This sensitivity is shown by the shadowed region in Fig. 6(b).

As expected, T_{CJ}, P_{CJ}, and impulse I peak near the stoichiometric ratio, where the chemical energy release is maximised, and decrease for leaner or richer mixtures. Meanwhile, the detonation speed V_{CJ} increases monotonically with H_2 concentration due to a lower average molecular weight and thus higher sound speed behind the wave (Lee and Kim, 1999). The CESE method, using both mechanisms, captures these trends well.

Up to 40 vol% H_2, the predicted V_{CJ} remains close to the theoretical value (within 1% error). Beyond this point, the reduced mechanism significantly overestimates the detonation speed (≈ 3%). Similarly, T_{CJ} is overpredicted at high H_2 concentrations by both mechanisms, with more pronounced errors (up to 6%) for the reduced model above 40 vol%.

P_{CJ} is generally well predicted, with small discrepancies arising from the arbitrary selection of the CJ point at 10 μs, since the detonation products continuously expand after that.

Impulse I is consistently underestimated due to the unresolved induction zone, as discussed in Section 3.1.1. This underestimation becomes more pronounced near the detonability limits (13% error), where induction times are longer. Consequently, for applications requiring accurate impulse predictions, particularly in structural analysis, the CESE method with a relatively coarse mesh is best suited to mixtures within the 25–40 vol% of H_2 range.

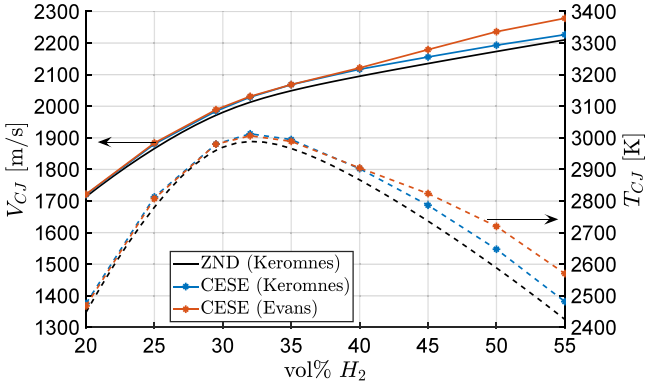

(a) CJ speed and temperature

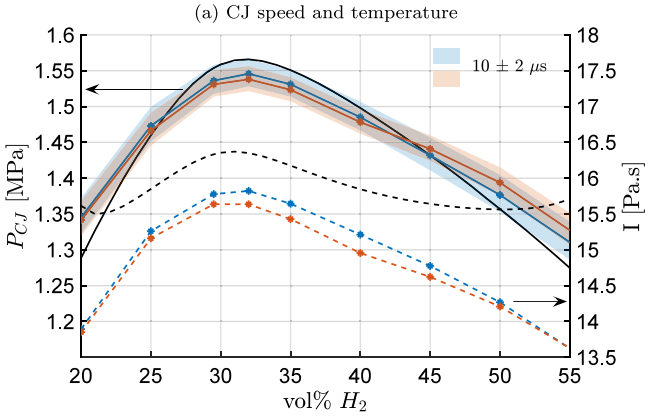

(b) CJ pressure and specific impulse. The shaded area shows P_{CJ} taken at 10±2 μs.

Fig. 6. CJ properties (after 10 μs) vs. initial H_2 concentration. P_0 = 1 bar, T_0 = 300 K.

3.1.3. Effect of mesh size

The mesh size, h, significantly influences the accuracy of CESE predictions. To evaluate this effect, simulations were performed using the reduced mechanism (Evans and Schexnayder, 1980), fixed initial conditions, and a structured mesh with a resolution from 2.0 mm to 0.2 mm. 7(a) compares the predicted pressure and specific impulse profiles against the ZND solution, while Fig. 7(b) shows the corresponding errors and computational time.

The CJ properties – P_{CJ}, T_{CJ}, and V_{CJ} – are relatively insensitive to mesh resolution, remaining within 3% error. Only V_{CJ} increases slightly with a coarser mesh. This is expected, as these values correspond to a thermodynamic equilibrium state derived from the Rankine–Hugoniot conditions and do not depend on transient aspects affected by mesh resolution.

In contrast, peak pressure, P_{vN}, is strongly affected by mesh size. The vN state represents a discontinuous shock-compressed region, which requires an extremely fine mesh to be fully resolved. Coarser meshes tend to smear the shock front, leading to a reduced P_{vN}, with errors reaching up to 23% for a 2 mm mesh.

Impulse errors remain below 5% at stoichiometric conditions (Fig. 7(b)). Interestingly, this error does not decrease with mesh refinement (within h = 0.2–2 mm). A finer mesh, while better resolving the shock front, leads to earlier ignition due to the unresolved induction zone, causing the pressure to decay prematurely and reducing the total impulse. Conversely, coarser meshes artificially extend the reaction zone and peak pressure duration, which increases impulse and partially compensates for the missing induction zone.

Despite being a numerical artefact, this effect can be exploited: coarser meshes in the range of 1–2 mm yield more accurate impulse

Table 2
Summary of validation results showing average detonation properties over the test section and respective errors.

Variable	25% H_2			29.6% H_2			40% H_2		
	Exp.	Sim.	Err. %	Exp.	Sim.	Err. %	Exp.	Sim.	Err. %
$P1_{peak}$ [MPa]	2.63	1.70	35.6	3.10	1.70	45.0	2.57	1.69	34.3
$P2_{peak}$ [MPa]	1.57	1.18	25.3	1.44	1.15	20.4	1.59	1.19	25.1
P_{QS} [MPa]	0.48	0.48	0.4	0.52	0.51	2.1	0.50	0.51	1.1
$I1$ [Pa s]	46.3	42.3	8.7	45.6	37.3	18.1	43.0	37.0	14.0
$I2$ [Pa s]	45.9	48.3	5.2	42.4	46.6	9.9	43.4	47.8	10.1
V [m/s]	1795	1794	0.1	1890	1882	0.4	1992	2028	1.8

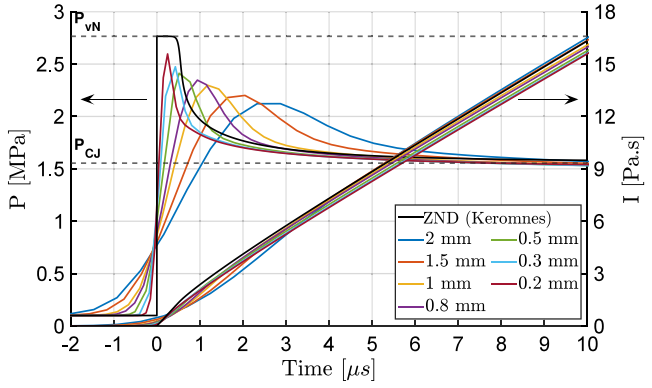

(a) Pressure and specific impulse.

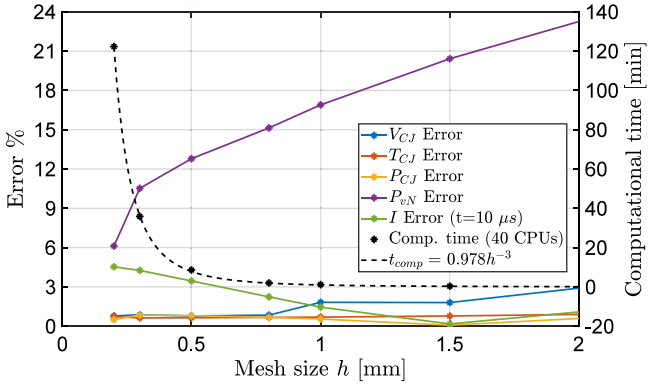

(b) Errors relative to the ZND solution vs. mesh size, and respective computational time. N_{cells} = 2.5, 4.7, 10, 15, 40, 110, 250 thousand (for h =2-0.2 mm). Runtime was 0.6 ms.

Fig. 7. Comparison between CESE and ZND detonation front solutions for meshes with 2–0.2 mm. Obtained using Evans reduced mechanism at stoichiometric conditions and P_0 = 1 bar, T_0 = 300 K.

predictions, while compromising P_{vN}, a less critical parameter for structural loading (see Section 3.2.1).

The simulations were performed using MPI parallelisation on 40 Intel Xeon E5-2640 (2.4 GHz) CPU cores, with a total physical runtime of 0.6 ms. Assuming a constant Courant number, C_{CFL}, the explicit time step is approximately $\Delta t = C_{CFL} \times h/V_{CJ}$. The number of time steps is inversely proportional to the step size, $N_{steps} \propto \Delta t^{-1} \propto h^{-1}$. On the other hand, the computational time per time step scales with the total number of cells in the mesh, which, for a 2D domain, is $N_{cells} \propto h^{-2}$. Therefore, the total computational time is $t_{comp} \propto N_{steps} \times N_{cells} \propto h^{-3}$. Fig. 7(b) shows that $t_{comp} = 0.978\,h^{-3}$ correctly fits the computational time. Extrapolating this for a mesh size of h = 2 μm, corresponding to the smallest step size taken by the ZND solver to resolve the induction zone, yields an estimated computational time of 230 years.

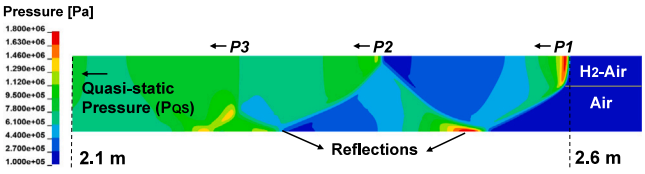

Fig. 8. Pressure contours obtained for 29.6 vol% H_2 in the test section.

3.2. Validation against experiment

Building on the previous results, the CESE-chemistry model, described in Section 2.2, is now validated against a full-scale detonation experiment by Rudy et al. (2017).

To balance accuracy and computational cost, the 7-species reduced mechanism by Evans and Schexnayder (1980) is used with a structured mesh of 1 mm. As shown in Section 3.1, this setup accurately predicts key detonation front properties (except for P_{vN}) within the 25–40 vol% H_2 range of the experiment.

Simulations were run on 12 CPUs using shared-memory parallelisation, requiring 28–29 h to simulate 1.5 ms of physical time. This confirms that full-scale detonation modelling with the CESE-chemistry method is feasible with adequate computational resources. Around 90% of the computational cost was attributed to the chemistry solver, highlighting the importance of using reduced reaction mechanisms whenever possible.

Fig. 8 shows the detonation pressure contours in the test section, near PS5 location. The detonation front propagates along the H_2-air upper channel, while its combustion products expand into the air-only region below. The downward shock reflects off the lower wall, creating a second pressure pulse at the upper wall, followed by weaker reflections until the pressure stabilises. The three pressure pulses are labelled $P1$, $P2$, and $P3$. The quasi-static pressure, P_{QS}, refers to the pressure of the expanded gas behind the three main pulses, which becomes approximately constant.

Fig. 9 compares the simulated (Sim.) and experimental (Exp.) pressure histories at sensor locations PS1 through PS5, for 25, 29.6, and 40 vol% H_2. Specific impulse histories are shown in Fig. 10. $P3$ is a smaller, smoother pulse, and it is not clearly distinguishable in all sensors or in the experimental data. Therefore, the analysis focuses on $P1$ and $P2$, labelled on the PS3 time–history for reference.

To facilitate comparison, the simulation time is shifted by 0.24, 0.23, 0.21 ms, and the experimental time by 0.19, 0.09, 0.08 ms (respectively for 25, 29.6, and 40 vol%). This way, the detonation arrival at PS1 is synchronised with t = 0 ms.

Overall, the simulation shows good agreement with experimental results. The model captures the fast pressure drop caused by expansion into the air region and the three main pulses observed in PS3-PS5. Pressure histories at PS1 and PS2 differ from the other sensors, as expected, because they are located in the acceleration section and the transition to the test section.

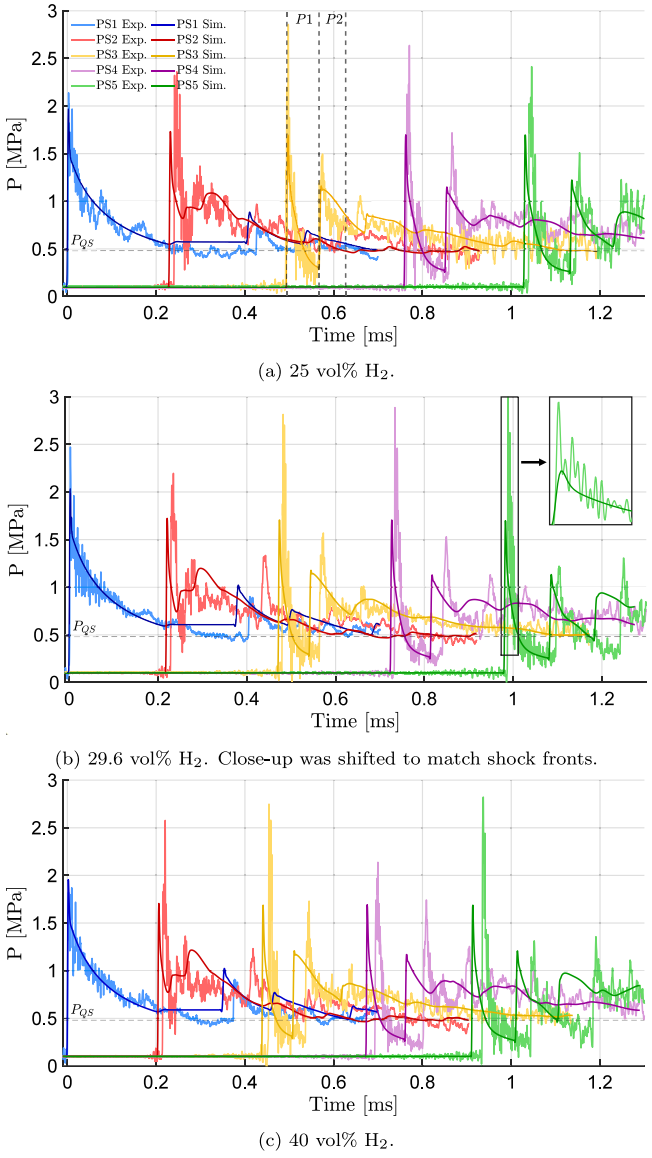

(a) 25 vol% H_2.

(b) 29.6 vol% H_2. Close-up was shifted to match shock fronts.

(c) 40 vol% H_2.

Fig. 9. Comparison between experimental and simulation pressure history at PS1-PS5 sensors, for 25, 29.6 and 40 vol% H_2. Data synchronised at PS1.

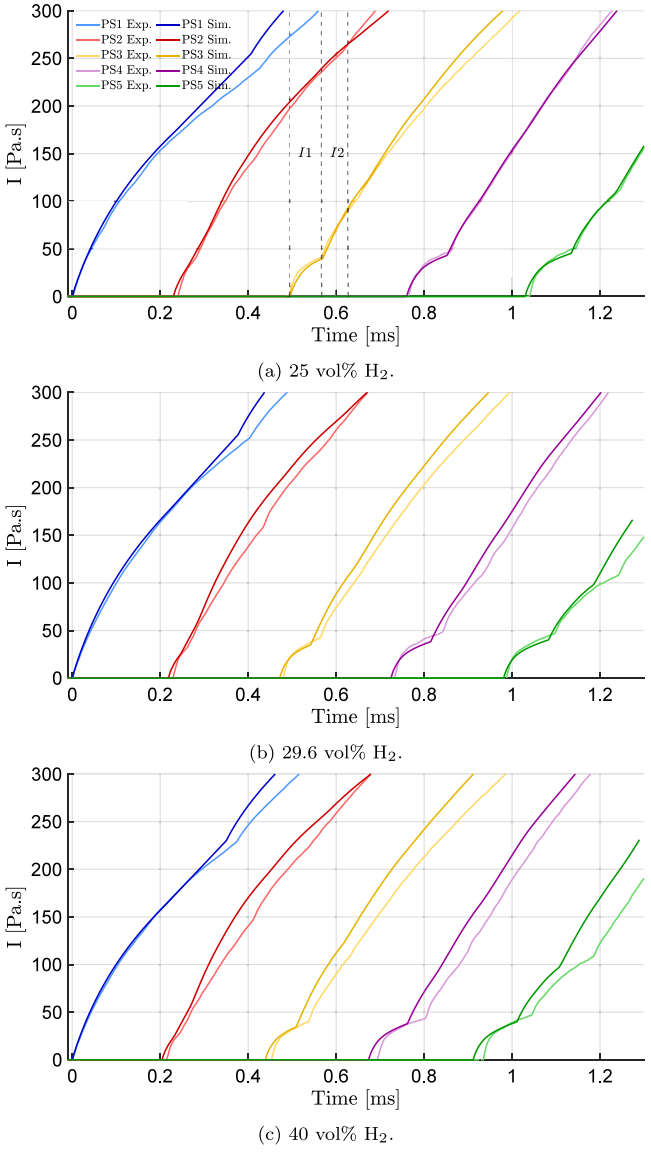

(a) 25 vol% H_2.

(b) 29.6 vol% H_2.

(c) 40 vol% H_2.

Fig. 10. Comparison between experimental and simulation specific impulse history at PS1-PS5 sensors, for 25, 29.6 and 40 vol% H_2. Data synchronised at PS1.

The shorter acceleration section in the model (0.7 m) causes pressure at PS1 to stabilise at a higher value relative to the experiment (see Fig. 9). Nevertheless, the results in the test section (PS2-PS5) are less sensitive to this length. When changing to 0.6 m or 0.8 m, the average impulse and peak pressure vary less than 0.9% for pulse P1 and 2.7% for pulse P2, with respect to the 0.7 m section. The detonation speed also varies slightly (0.4%).

Table 2 summarises the peak pressures ($P1_{\text{peak}}$, $P2_{\text{peak}}$) and impulses ($I1$, $I2$) for the first and second pulses ($P1$, $P2$), along with their errors relative to experimental data. Impulse $I1$ is measured from the first to the second pressure peak, while $I2$ is integrated over 0.06 ms following the second peak (see Fig. 10(a)) since the end of $P2$ is not always clear in the experimental data. Results are averaged over sensors PS3-PS5, where both pulses are clearly identifiable. The quasi-static pressure P_{QS} is defined as the mean pressure at PS2 and PS3 for $t >$ 1.1 ms. The detonation speed V is the average over the test section.

The quasi-static pressure, $P_{QS} \approx 0.5$ MPa, is within 2.1% error for all cases. The simulation also accurately captures the pressure decay following the primary pulses, indicating a reliable representation of the expanding combustion products.

Predicted detonation speeds match experimental values closely, with a maximum error of 1.8% at 40 vol% H_2, consistent with the overprediction observed in one-dimension (Fig. 6). This small discrepancy leads to a time shift in the simulations, where the detonation front arrives slightly earlier than in the experimental measurements.

Both measured and simulated speeds are 3%–5% below the theoretical $V_{CJ} = 1972$ m/s, due to the detonation products expansion into the air region – a phenomenon correctly captured by the model and in agreement with Rudy et al. (2017).

Because of that, detonation slows down from the acceleration section to the test section, causing the peak pressure $P1_{\text{peak}}$ to also decrease from PS1 to PS2 in the simulation results (Fig. 9). However, the measured $P1_{\text{peak}}$ values are much larger than predicted by the model, occasionally exceeding P_{vN}, and show significant variability.

The larger $P1_{\text{peak}}$ values are attributed to the complex 3D detonation cell structure, where the intersections between transverse and

leading shocks form triple points, producing local pressure spikes well above P_{vN}, as concluded by Smirnov et al. (2024). These fluctuations are evident in the close-up view of Fig. 9(b). When averaged over the cross-section, pressure fluctuations reduce and approach the ZND prediction (Smirnov et al., 2024).

The boundary layer can also increase the peak pressure value near the wall, due to the no-slip condition (Chinnayya et al., 2013). While this effect is localised, it affects the experimental data since the sensors are placed flush to the wall.

The present model assumes a planar detonation front, slip conditions, and does not resolve cellular structure. Combined with shock smearing caused by the coarse mesh (Fig. 7(a)), these simplifications lead to significant underprediction of $P1_{\text{peak}}$ and $P2_{\text{peak}}$.

Resolving the cellular structure requires substantially finer resolution than used here. Sharpe (2001) recommends at least 20 points per induction length, while recent studies often employ 40–50 points/Δ_i (Weng et al., 2025; Sankar et al., 2025). With Δi=0.2 mm, obtained in Section 3.1.1, such resolution is computationally prohibitive for large simulations. Note that this would yield hundreds of points along a single detonation cell (with an average size of λ = 8 mm from Rudy et al. (2017)).

Impulse histories in Fig. 10 follow the experimental trends, aside from the consistent time shift. The arrival of each pressure pulse causes a sudden increase in impulse. Table 2 shows that $I1$ is underestimated by 8.7–18.1%, with the smallest error at 25 vol% H_2. Several factors contribute to this. First, the predicted $P1$ duration is shorter because $P2$ propagates faster and arrives earlier in the simulation, reducing $I1$ by about 5%. Second, the detonation front is a complex cellular structure with transverse waves, increasing the overall measured impulse relative to the planar wave model. A more representative comparison would average experimental pressures over a finite distance from the wall, but such data are not available. Third, the CESE method slightly underpredicts impulse compared to ZND (see Section 3.1.1), though this is a smaller effect.

The compressibility factor Z describes the deviation of a real gas from the ideal behaviour, for which Z=1. At the CJ state (P_{CJ} = 1.55 MPa., T_{CJ} = 2961 K), the compressibility is Z=1.0007 and Z=1.002 for H_2O and N_2 (the major species after combustion), respectively (Bell et al., 2014). This corresponds to an error of less than 0.2% in pressure stemming from the ideal gas assumption, not enough to justify the impulse underprediction (in the order of 10%).

The second impulse $I2$ is predicted within 10% error for all cases and is also most accurate at 25 vol% H_2. This confirms the model's ability to capture not only the detonation front but also complex shock reflections within confined domains. The fact that $I1$ and $I2$ are of similar magnitude (Table 2) highlights the significant role of reflected shocks in structural loading from confined detonations.

3.2.1. Effect on structural deformation

While P_{peak} is often used as a measure of detonation strength, it is not the most relevant parameter in structural analysis. The duration, t_d, of pressure pulses caused by H_2-air detonations is extremely short, in the order of 10^{-4} s (See Fig. 9). If t_d is much smaller than the structure's natural period, the peak pressure will decay before it deforms significantly (Hetherington and Smith, 2014).

This is called an impulsive loading regime, where the total impulse I – not the peak pressure – governs the mechanical response (Chung Kim Yuen et al., 2017; Hetherington and Smith, 2014). In this regime, the impulse imparts a sudden velocity to the structure (kinetic energy), which is then converted into deformation (strain energy). Therefore, an accurate prediction of impulse is more critical than resolving the peak pressure when evaluating blast-loaded structural response.

The final deformation of thin plates subjected to blast loads scales approximately linearly with the applied impulse, for a fixed geometry and material (Chung Kim Yuen et al., 2017). Thus, the relative error in the predicted deformation is expected to be in the same order as the impulse.

In stoichiometric conditions, the experimental and predicted impulses are $I1_{exp}$ = 45.6 Pa s and $I1_{sim}$ = 37.3 Pa s (from Table 2), corresponding to the larger error of 18.1%. Take, as an example, a circular stainless steel plate with ρ = 8000 kg/m^3, σ_y = 215 MPa, R = 200 mm and t = 1 mm (density, yield stress, radius and thickness). From Chung Kim Yuen et al. (2017), the blast-loaded plate would deform by δ_{exp} = 3.3 mm and δ_{sim} = 2.7 mm, a difference of 16.5%.

This simple analysis can help define the practical limitations of this methodology, given a requirement in deformation accuracy.

4. Conclusions

This study presented a methodology for predicting blast loads from hydrogen–air detonations with varying compositions, using the CESE-chemistry solver in LS-DYNA. The model assumed a 2D geometry, planar wave front, inviscid flow, and finite-rate chemistry, employing four different reaction mechanisms.

As a first step, a long shock tube configuration was simulated to approximate one-dimensional conditions and compare the computed detonation front with the theoretical ZND solution. The key findings are:

1. Reduced (7 species) and detailed (10, 19 species) reaction mechanisms produced similar results near stoichiometric conditions. Computational time scales with the square of the number of species, so reduced mechanisms are significantly more efficient for large simulations.
2. One-dimensional detonation speed V_{CJ}, pressure P_{CJ}, and temperature T_{CJ} were predicted within 1%–2% accuracy up to 40 vol% H_2, beyond which the reduced mechanism begins to deviate.
3. Impulse at the detonation front is underpredicted (within 5%, in stoichiometric conditions) regardless of mesh refinement, due to the unresolved induction zone.
4. Coarse meshes (with 1–2 mm size) significantly smear the shock front, causing up to 23% error in peak pressure P_{vN}; this error improves with finer resolution. On the contrary, the CJ state is relatively insensitive to mesh resolution.
5. The computational time scales with the inverse cube of the mesh size.

Building on the shock tube results, the 2D model was validated against a full-scale hydrogen–air detonation experiment in a 3-metre confined chamber, with H_2 concentrations of 25, 29.6, and 40 vol%. For computational efficiency, the reduced mechanism with 7 species and a 1 mm mesh size was used. Direct ignition was employed to initiate a planar detonation front, bypassing the deflagration-to-detonation transition (DDT) process. Comparison with experimental data showed:

1. Overall good agreement in pressure histories, including accurate prediction of two main pressure pulses associated with the detonation front and wall reflections.
2. Detonation speed (which deviated from the theoretical V_{CJ}) and quasi-static pressure were predicted within 2% error across all cases.
3. The detonation cell structure was not captured due to the planar wave assumption and coarse mesh. This contributes to large peak pressure errors (up to 45%) and moderate impulse errors (up to 18%).
4. The second impulse is captured within 10% error, showing the model's ability to predict shock wave reflections in confined environments.
5. While errors obtained for 29.6 vol% and 40 vol% are overall similar, the model performed particularly well at lean conditions (25 vol% H_2).

Table A.3
Effect of Courant–Friedrichs–Lew number C_{CFL} and the relaxation parameter ϵ on results stability and accuracy. Obtained in stoichiometric conditions and 0.3 mm element size.

Solver Parameters		Errors %				Obs.
ϵ	C_{CFL}	P_{vN}	P_{CJ}	T_{CJ}	V_{CJ}	
0.5	0.99	10.5	0.8	0.6	0.9	–
0.5	0.8	16.8	0.8	0.6	0.9	–
0.5	0.5	23.3	0.7	0.7	0.9	–
0.01	0.99	–	–	–	–	No convergence
0.1	0.99	29.5	1.6	0.5	0.7	Numerical oscillations
5	0.99	10.1	0.6	0.7	0.8	–
10	0.99	12.5	0.5	0.7	0.9	–

Table B.4
H_2-air mechanism by Evans et al. with 7[a] species and 8 reactions (Evans and Schexnayder, 1980). Units: cm^3/mol/s/cal.

No.	Reaction	A	β	E
1	$H_2 + M = H + H + M$[b]	5.5E+18	−1.00	1.033E+5
2	$O_2 + M = O+O+M$	7.2E+18	−1.00	1.179E+5
3	$H_2O+M=OH+H+M$	5.2E+21	−1.50	1.180E+5
4	$OH+M=O+H+M$	8.5E+18	−1.00	1.010E+5
5	$H_2O+O=OH+OH$	5.8E+13	0.00	1.800E+4
6	$H_2O+H=OH+H_2$	8.4E+13	0.00	2.010E+4
7	$O_2+H=OH+O$	2.2E+14	0.00	1.680E+4
8	$H_2+O=OH+H$	7.5E+13	0.00	1.110E+4

[a] 7 species: H, O, OH, H_2, O_2, H_2O, N_2 (bath gas).
[b] Three-body efficiencies: $\epsilon_{H_2} = 2.5$, $\epsilon_{H_2O} = 10$.

Table B.5
H_2-air mechanism by Drummond et al. with 7[a] species and 7 reactions (Drummond et al., 1986). Units: cm^3/mol/s/cal.

No.	Reaction	A	β	E
1	$H_2 + O_2 = 2OH$	1.70E+13	0.0	4.816E+04
2	$H+O_2= OH+O$	1.42E+14	0.0	1.640E+04
3	$OH+H_2=H_2O+H$	3.16E+7	1.8	3.031E+03
4	$O+H_2=OH+H$	2.07E+14	0.0	1.375E+04
5	$2OH=H_2O+O$	5.5E+13	0.00	7.001E+03
6	$H+OH+M=H_2O+M$[b]	2.21E+22	−2.00	0.0
7	$2H+M=H_2+M$	6.53E+17	−1.00	0.0

[a] 7 species: H, O, OH, H_2, O_2, H_2O, N_2 (bath gas).
[b] Three-body efficiencies: $\epsilon_{H_2} = 2.5$, $\epsilon_{H_2O} = 10$.

While this approach does not resolve the detonation cell structure, it accurately captures the key features relevant to blast load prediction. The methodology is therefore validated for hydrogen–air detonations across a range of concentrations, offering a practical and scalable tool for safety assessments in confined environments.

CRediT authorship contribution statement

Simão M. Martins: Writing – original draft, Visualization, Validation, Software, Methodology, Investigation, Formal analysis. **Alexander van Zuijlen:** Writing – review & editing, Supervision. **Saullo G.P. Castro:** Writing – review & editing, Supervision, Resources, Project administration, Funding acquisition, Data curation, Conceptualization.

Declaration of competing interest

The authors declare that they have no known competing financial interests or personal relationships that could have appeared to influence the work reported in this paper.

Acknowledgement

This research is conducted within the research and innovation programme Luchtvaart in Transitie, which is co-funded by the Netherlands National Growth Fund. It is part of the 'HAPSS Phase 2' project, and part of The CrashProof Knowledge Centre (CrashProofLab) (Castro, 2022).

Appendix A. CESE solver parameters

See Table A.3.

Appendix B. Reaction mechanisms

See Tables B.4 and B.5.

Appendix C. Thermodynamic properties

See Table C.6.

Data availability statement

All models and datasets generated and analysed during this study are publicly available (Martins et al., 2025).

Table C.6
Thermodynamic properties of species H_2, H, O_2, O, OH, H_2O and N_2 in NASA-polynomial format. Taken from the Explosion Dynamics Laboratory database, Calthec (Browne et al., 2024).

	Range	a_1	a_2	a_3	a_4	a_5	a_6	a_7
H_2	200–1000 K	2.344	7.980E−3	−1.948E−5	2.016E−8	−7.376E−12	−9.179E+2	0.683
	1000–6000 K	2.933	8.266E−4	−1.464E−7	1.541E−11	−6.888E−16	−8.131E+2	−1.024
H	200–1000 K	2.500	0	0	0	0	2.547E+4	−0.447
	1000–6000 K	2.500	0	0	0	0	2.547E+4	−0.447
O_2	200–1000 K	3.782	−2.997E−3	9.847E−6	−9.681E−9	3.244E−12	−1.064E+3	3.658
	1000–6000 K	3.661	6.564E−4	−1.411E−7	2.058E−11	−1.299E−15	−1.216E+3	3.415
O	200–1000 K	3.168	−3.279E−3	6.643E−6	−6.128E−9	2.113E−12	2.912E+4	2.052
	1000–6000 K	2.544	−2.732E−5	−4.190E−9	4.955E−12	−4.796E−16	2.923E+4	4.922
OH	200–1000 K	3.992	−2.401E−3	4.617E−6	−3.879E−9	1.363E−12	3.699E+3	−0.104
	1000–6000 K	2.839	1.107E−3	−2.940E−7	4.207E−11	−2.423E−15	3.698E+3	5.845
H_2O	200–1000 K	4.199	−2.036E−3	6.520E−6	−5.488E−9	1.772E−12	−3.029E+4	−0.849
	1000–6000 K	10.743	2.973E−3	−7.738E−7	9.443E−11	−4.269E−15	−2.989E+4	6.883
N_2	200–1000 K	3.531	−1.237E−4	−5.030E−7	2.435E−9	−1.409E−12	−1.047E+3	2.967
	1000–6000 K	2.953	1.397E−3	−4.926E−7	7.860E−11	−4.608E−15	−9.239E+2	5.872

References

ANSYS, Inc., 2024. LS-DYNA Keyword User's Manual: Volume III (Multiphysics Solvers). URL: https://lsdyna.ansys.com/manuals/.

Bell, I.H., Wronski, J., Quoilin, S., Lemort, V., 2014. Pure and pseudo-pure fluid thermophysical property evaluation and the open-source thermophysical property library CoolProp. Ind. Eng. Chem. Res. 53 (6), 2498–2508. http://dx.doi.org/10.1021/ie4033999.

Browne, S.T., Ziegler, J.L., Bitter, N.P., Schmidt, B.E., Lawson, J., Shepherd, J.E., 2024. Sdtoolbox: Numerical Tools for Shock and Detonation Wave Modeling. Technical Report FM2018.001, California Institute of Technology, Pasadena, CA, URL: https://shepherd.caltech.edu/EDL/PublicResources/sdt/.

Castro, S.G.P., 2022. The CrashProof Knowledge Centre (CrashProofLab). Zenodo, http://dx.doi.org/10.5281/zenodo.11500722.

Chamberlain, G., Oran, E., Pekalski, A., 2019. Detonations in industrial vapour cloud explosions. J. Loss Prev. Process. Ind. 62, http://dx.doi.org/10.1016/j.jlp.2019.103918.

Chang, S.-C., 1995. The method of space-time conservation element and solution element—A new approach for solving the Navier-Stokes and Euler equations. J. Comput. Phys. (2), 295–324. http://dx.doi.org/10.1006/jcph.1995.1137.

Chen, D., Wu, C., Li, J., 2023. Assessment of modeling methods for predicting load resulting from hydrogen-air detonation. Process. Saf. Environ. Prot. 180, 752–765. http://dx.doi.org/10.1016/j.psep.2023.10.051.

Chinnayya, A., Hadjadj, A., Ngomo, D., 2013. Computational study of detonation wave propagation in narrow channels. Phys. Fluids 25 (3), 036101. http://dx.doi.org/10.1063/1.4792708.

Chung Kim Yuen, S., Nurick, G.N., Langdon, G.S., Iyer, Y., 2017. Deformation of thin plates subjected to impulsive load: Part III – an update 25 years on. Int. J. Impact Eng. 107, 108–117. http://dx.doi.org/10.1016/j.ijimpeng.2016.06.010.

Dorofeev, S.B., Sidorov, V.P., Dvoinishnikov, A.E., Breitung, W., 1996. Deflagration to detonation transition in large confined volume of lean hydrogen-air mixtures. Combust. Flame 104 (1), 95–110. http://dx.doi.org/10.1016/0010-2180(95)00113-1.

Drummond, J.P., Rogers, R.C., Hussaini, M.Y., 1986. A detailed numerical model of a supersonic reacting mixing layer. In: 22nd Joint Propulsion Conference. AIAA, Huntsville, Alabama.

Evans, J.S., Schexnayder, C.J., 1980. Influence of chemical kinetics and unmixedness on burning in supersonic hydrogen flames. AIAA J. 18 (2), 188–193. http://dx.doi.org/10.2514/3.50747.

Evro, S., Oni, B.A., Tomomewo, O.S., 2024. Carbon neutrality and hydrogen energy systems. Int. J. Hydrog. Energy 78, 1449–1467. http://dx.doi.org/10.1016/j.ijhydene.2024.06.407.

Fickett, W., Davis, W.C., 2000. Detonation: Theory and Experiment. Courier Corporation.

Grippon, E., Dorsselaer, N.V., Lapoujade, V., 2015. A Contribution to CESE method validation in LS-DYNA®. In: 10th European LS-DYNA Conference. LSTC, Wurzburg, Germany.

Groethe, M., Merilo, E., Colton, J., Chiba, S., Sato, Y., Iwabuchi, H., 2007. Large-scale hydrogen deflagrations and detonations. Int. J. Hydrog. Energy 32 (13), 2125–2133. http://dx.doi.org/10.1016/j.ijhydene.2007.04.016.

Haghgoo, M., Babaei, H., Mostofi, T., 2021. 2D numerical study on the deflection of thin steel plate subjected to gaseous detonation wave interaction. Int. J. Hydrog. Energy 46 (73), 36348–36368. http://dx.doi.org/10.1016/j.ijhydene.2021.08.146.

Hasslberger, J., Boeck, L.R., Sattelmayer, T., 2015. Numerical simulation of deflagration-to-detonation transition in large confined volumes. J. Loss Prev. Process. Ind. 36, 371–379. http://dx.doi.org/10.1016/j.jlp.2014.11.018.

Hetherington, J., Smith, P., 2014. Blast and Ballistic Loading of Structures. CRC Press, London, http://dx.doi.org/10.1201/9781482269277.

Huang, X., Weng, Z., Mével, R., Melguizo-Gavilanes, J., Chatelain, K.P., Vargas, J., Lacoste, D.A., 2025. Chemical kinetics uncertainty quantification on the dynamic detonation parameters for hydrogen–air mixtures. Combust. Flame 275, 114107. http://dx.doi.org/10.1016/j.combustflame.2025.114107.

IEA, 2023. Net zero roadmap: A global pathway to keep the 1.5 °C goal in reach. Technical Report, Paris, URL: https://www.iea.org/reports/net-zero-roadmap-a-global-pathway-to-keep-the-15-0c-goal-in-reach.

Im, K.-S., 2018. LNG combustion with LS-dyna CESE solvers. URL: https://www.slideshare.net/slideshow/lng-combustion-with-lsdyna-cese-solverspdf/266767152.

Im, K.-S., Joh, S.-T., Kim, C.-K., Chang, S.-C., Jorgenson, C., 2002. Application of the CESE method to detonation with realistic finite-rate chemistry. In: 40th AIAA Aerospace Sciences Meeting & Exhibit. American Institute of Aeronautics and Astronautics, Reno,NV,U.S.A., http://dx.doi.org/10.2514/6.2002-1020.

Jiang, Y., Wen, C.-Y., Zhang, D., 2020. Space–time conservation element and solution element method and its applications. AIAA J. 58 (12), 5408–5430. http://dx.doi.org/10.2514/1.J058928.

Kéromnès, A., Metcalfe, W.K., Heufer, K.A., Donohoe, N., Das, A.K., Sung, C.-J., Herzler, J., Naumann, C., Griebel, P., Mathieu, O., Krejci, M.C., Petersen, E.L., Pitz, W.J., Curran, H.J., 2013. An experimental and detailed chemical kinetic modeling study of hydrogen and syngas mixture oxidation at elevated pressures. Combust. Flame 160 (6), 995–1011. http://dx.doi.org/10.1016/j.combustflame.2013.01.001.

Kim, S., Jang, T., Oli, T., Park, C., 2023. Behavior of barrier wall under hydrogen storage tank explosion with simulation and TNT equivalent weight method. Appl. Sci. 13 (6), http://dx.doi.org/10.3390/app13063744.

Lee, S.-R., Kim, J.S., 1999. Structure and length of chemistry induction zone in hydrogen-air detonations. Korean J. Chem. Eng. 16 (2), http://dx.doi.org/10.1007/BF02706845.

Martins, S.M., van Zuijlen, A.H., Castro, S.G.P., 2025. Dataset for Modelling confined hydrogen-air detonations with the conservation element/solution element method for varying initial compositions. Dataset on Zenodo http://dx.doi.org/10.5281/zenodo.17788156.

Mcbride, B.J., Gordon, S., Reno, M.A., 1993. Coefficients for Calculating Thermodynamic and Transport Properties of Individual Species. Technical Report NASA-TM-4513, National Aeronautics and Space Administration.

Olm, C., Zsély, I.G., Pálvölgyi, R., Varga, T., Nagy, T., Curran, H.J., Turányi, T., 2014. Comparison of the performance of several recent hydrogen combustion mechanisms. Combust. Flame 161 (9), 2219–2234. http://dx.doi.org/10.1016/j.combustflame.2014.03.006.

Oran, E., Gamezo, V., 2007. Origins of the deflagration-to-detonation transition in gas-phase combustion. Combust. Flame 148, 4–47. http://dx.doi.org/10.1016/j.combustflame.2006.07.010.

Poinsot, T., Veynante, D., 2005. Theoretical and Numerical Combustion, second ed. RT Edwards, Inc.

Rokhy, H., Mostofi, T., 2023. Tracking the explosion characteristics of the hydrogen-air mixture near a concrete barrier wall using CESE IBM FSI solver in LS-DYNA incorporating the reduced chemical kinetic model. Int. J. Impact Eng. 172, http://dx.doi.org/10.1016/j.ijimpeng.2022.104401.

Rokhy, H., Soury, H., 2019. Fluid structure interaction with a finite rate chemistry model for simulation of gaseous detonation metal-forming. Int. J. Hydrog. Energy 44 (41), 23289–23302. http://dx.doi.org/10.1016/j.ijhydene.2019.07.030.

Rokhy, H., Soury, H., 2022. Investigation of the confinement effects on the blast wave propagated from gas mixture detonation utilizing the CESE method with finite rate chemistry model. Combust. Sci. Technol. 194 (14), 3003–3020. http://dx.doi.org/10.1080/00102202.2021.1905632.

Rudy, W., Dziubanii, K., Zbikowski, M., Teodorczyk, A., 2017. Experimental determination of critical conditions for hydrogen-air detonation propagation in partially confined geometry. Int. J. Hydrog. Energy 42 (11), 7366–7373. http://dx.doi.org/10.1016/j.ijhydene.2016.04.056.

Sankar, V., Chatelain, K.P., Lacoste, D.A., 2025. Evaluation of chemical kinetic models for simulations of hydrogen detonations by comparison with experimental data. Appl. Energy Combust. Sci. 21, 100306. http://dx.doi.org/10.1016/j.jaecs.2024.100306.

Schmitt, R.G., Butler, P.B., 1995. Detonation properties of gases at elevated initial pressures. Combust. Sci. Technol. 106 (1–3), 167–191. http://dx.doi.org/10.1080/00102209508907773.

Sharpe, G.J., 2001. Transverse waves in numerical simulations of cellular detonations. J. Fluid Mech. 447, 31–51. http://dx.doi.org/10.1017/S0022112001005535.

Smirnov, N.N., Nikitin, V.F., Mikhalchenko, E.V., Stamov, L.I., Tyurenkova, V.V., 2024. Modelling cellular structure of detonation waves in hydrogen-air mixtures. Int. J. Hydrog. Energy 49, 495–509. http://dx.doi.org/10.1016/j.ijhydene.2023.08.184.

Smith, G., Golden, D., Frenklach, M., Moriarty, N., Eiteneer, B., Goldenberg, M., Bowman, C., Hanson, R., Song, S., Gardiner, W., Lissianski, V., Qin, Z., 1999. GRI-Mech 3.0. Technical Report, URL: http://combustion.berkeley.edu/gri-mech/.

United States Department of the Army, 1986. Fundamentals of protective design for conventional weapons. In: US Department of the Army Technical Manual, no. TM5-855-1, Headquarters, Dept. of the Army, Washington, DC.

Warnatz, J., Maas, U., Dibble, R.W., 1996. Combustion, fourth ed. Springer, Berlin, Heidelberg, http://dx.doi.org/10.1007/978-3-642-97668-1.

Wen, J.X., Hecht, E.S., Mevel, R., 2025. Recent advances in combustion science related to hydrogen safety. Prog. Energy Combust. Sci. 107, http://dx.doi.org/10.1016/j.pecs.2024.101202.

Wen, C.-Y., Jiang, Y., Shi, L., 2023. Space–Time Conservation Element and Solution Element Method: Advances and Applications in Engineering Sciences. Springer Nature, Singapore, http://dx.doi.org/10.1007/978-981-99-0876-9.

Wen, J.X., Marono, M., Moretto, P., Reinecke, E.-A., Sathiah, P., Studer, E., Vyazmina, E., Melideo, D., 2022. Statistics, lessons learned and recommendations from analysis of HIAD 2.0 database. Int. J. Hydrog. Energy 47 (38), 17082–17096. http://dx.doi.org/10.1016/j.ijhydene.2022.03.170.

Weng, Z., Mével, R., 2022. Real gas effect on steady planar detonation and uncertainty quantification. Combust. Flame 245, 112318. http://dx.doi.org/10.1016/j.combustflame.2022.112318.

Weng, Z., Mével, R., Ren, Z., Shuai, S., 2025. Structure and dynamics of two-dimensional cellular detonation in a high-pressure H2-O2-Ar mixture. Combust. Flame 282, 114498. http://dx.doi.org/10.1016/j.combustflame.2025.114498.

Yanez, J., Kuznetsov, M., Souto-Iglesias, A., 2015. An analysis of the hydrogen explosion in the Fukushima-Daiichi accident. Int. J. Hydrog. Energy 40 (25), 8261–8280. http://dx.doi.org/10.1016/j.ijhydene.2015.03.154.